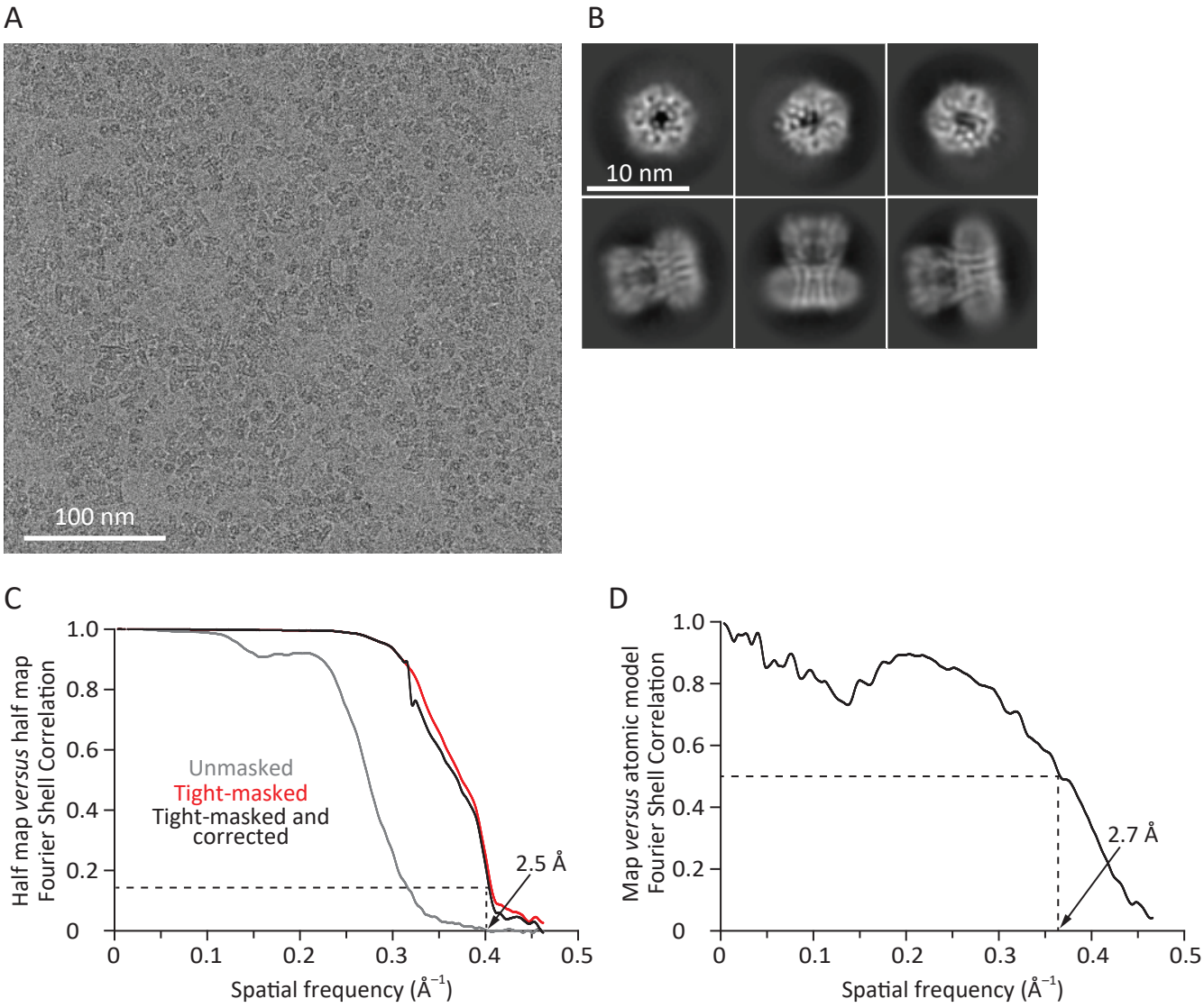

Fig. S1. Unliganded ELIC in SMA nanodiscs: cryo-EM micrographs, 2D class averages, and Fourier Shell Correlation (FSC) plots. (*A*) Representative micrograph with defocus 1.62 Å. (*B*) Selected 2D class averages. (*C*) FSC curves computed between independently refined half maps ("gold-standard" procedure). The global resolution was estimated using the 1/7 (≈ 0.143) cut-off criterion (1) upon application of a tight soft-edged mask and high-resolution noise substitution (2). (*D*) FSC curve computed between the sum of experimental half maps and a noise-free map calculated from the ELIC–SMA atomic model. A soft-edged mask was applied to the experimental map before computation of the curve. The resolution at which the map–model FSC equals 0.5 (2.7 Å) is similar to the global resolution of the 3D reconstruction calculated from the half maps (2.5 Å), as expected from the theoretical relationship between full maps, half maps, noiseless maps, and correctly built atomic models (1).

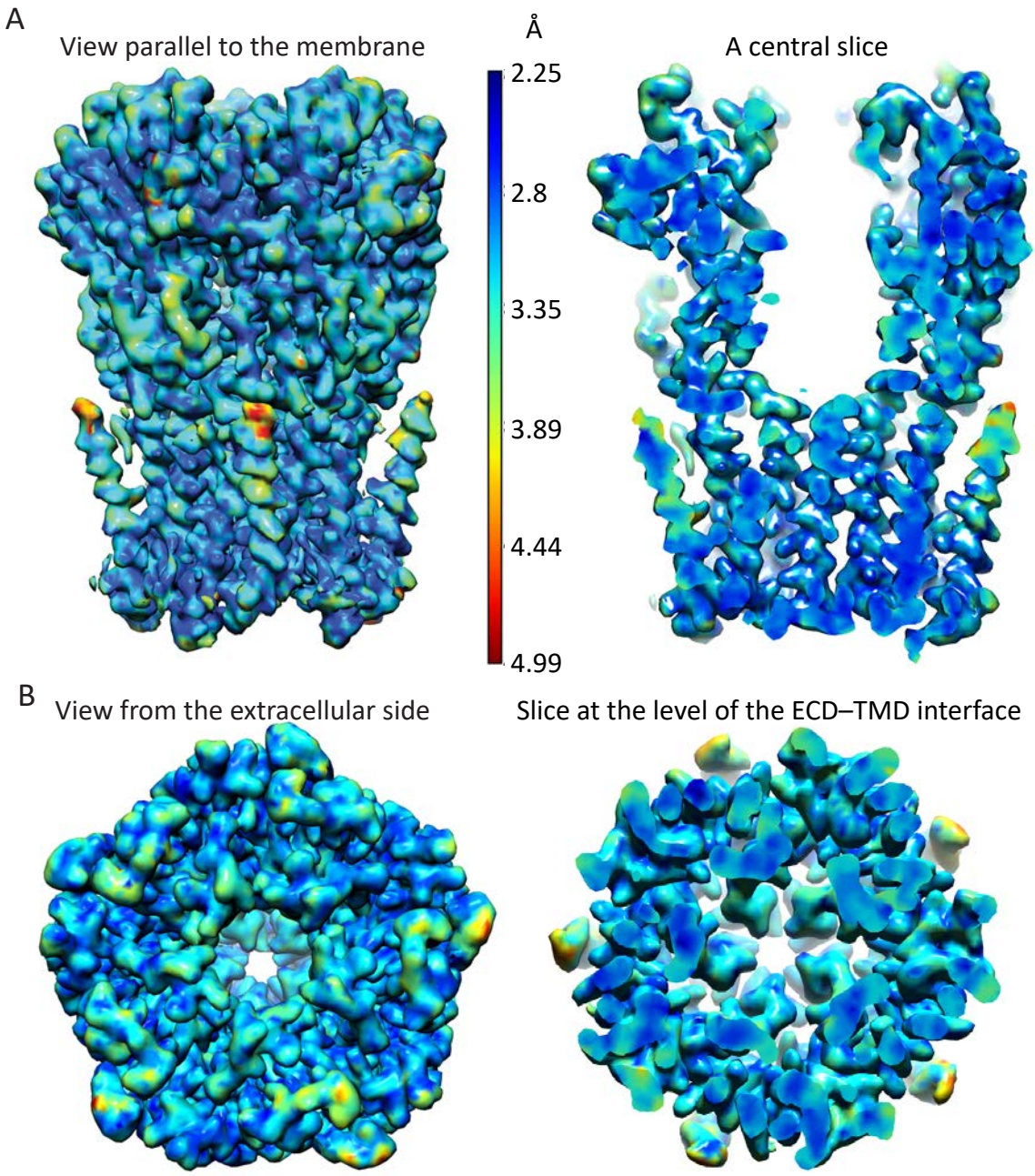

Fig. S2. Local-resolution map. (*A*, *B*) Different views of the 3D reconstruction of unliganded ELIC–SMA colored according to local resolution (display level = 0.57). Local resolution was estimated with MonoRes (3) in Xmipp/Scipion 2.0 (4) using the (unfiltered and unsharpened) sum of experimental half maps and a binary mask. The latter was created by loosely thresholding the former (level = 0.22) in an attempt to exclude voxels occupied by protein, bound phospholipids, and other nanodisc components from the noise-only volume.

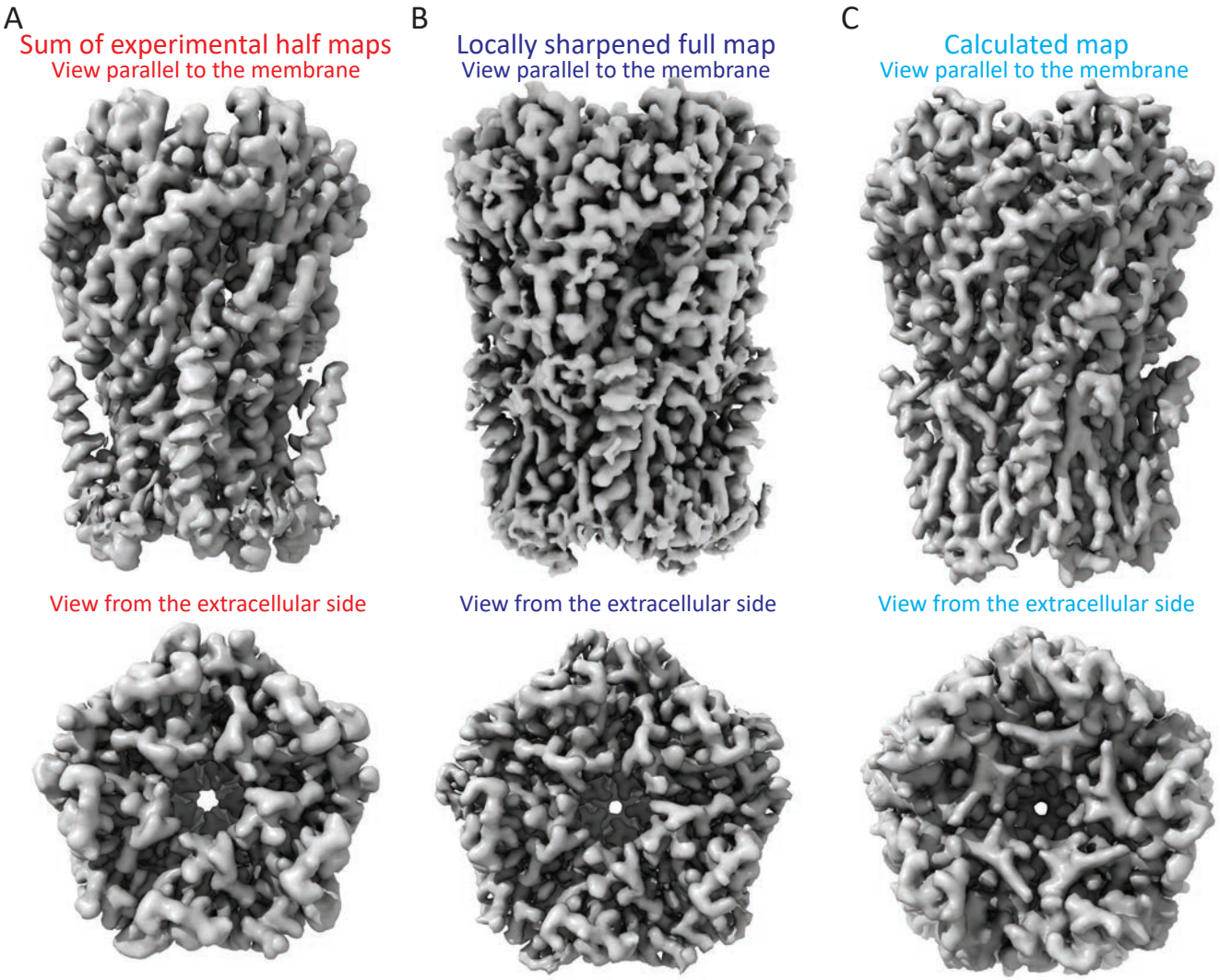

Fig. S3. Effect of local sharpening. (*A*–*C*) Different views of the sum of experimental half maps, the locally sharpened map, and a map calculated from the atomic model. Local sharpening was performed with LocalDeblur (5) in Xmipp/Scipion 2.0 (4) on the basis of the local-resolution map in *SI Appendix*, Fig. S2.

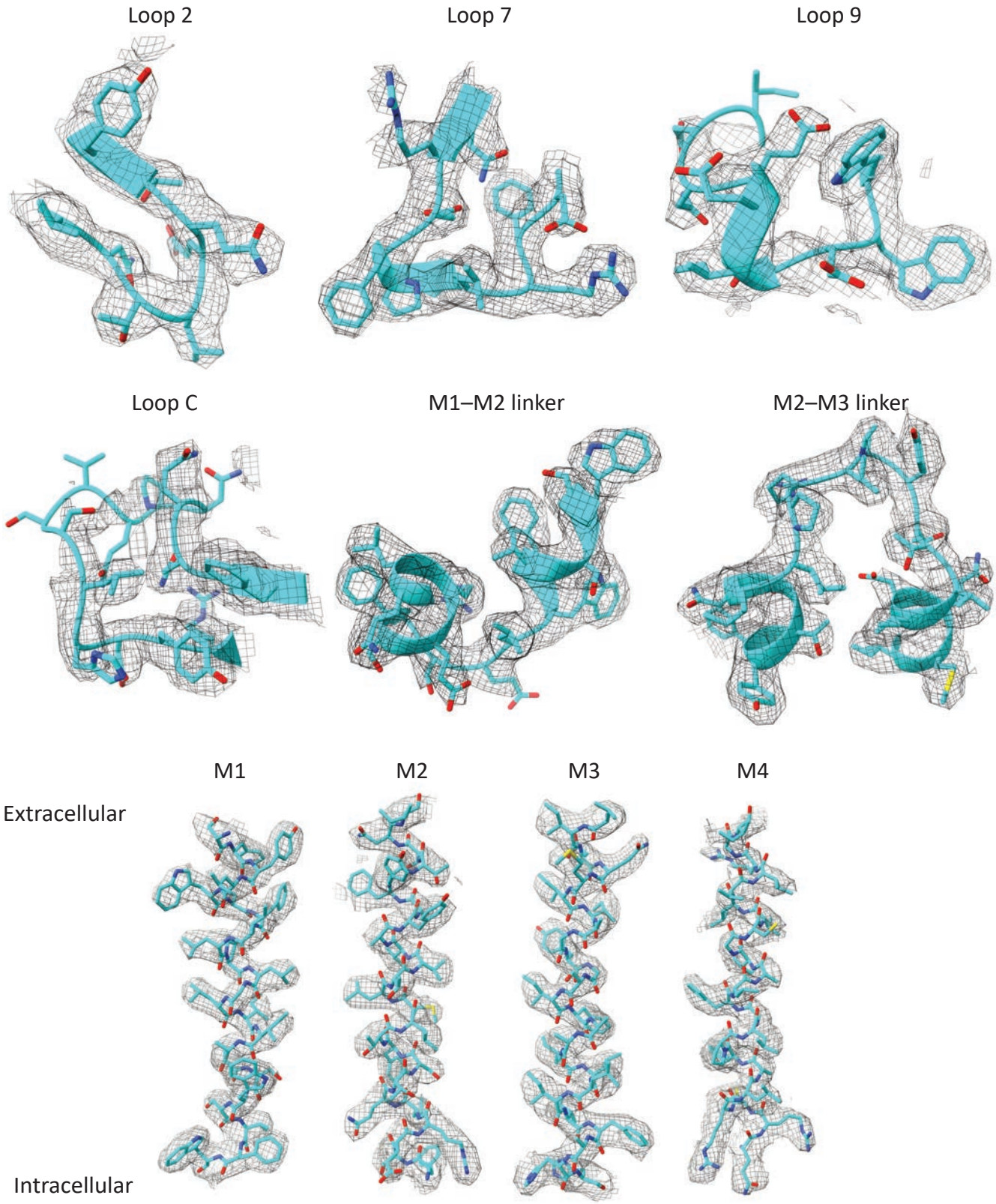

Fig. S4. Map–model fit. Different regions of the unliganded ELIC–SMA atomic model and corresponding densities. The display level is 0.8 for the M4 α-helix, and 1.2 for all other regions. Molecular images were prepared with Chimera X (6).

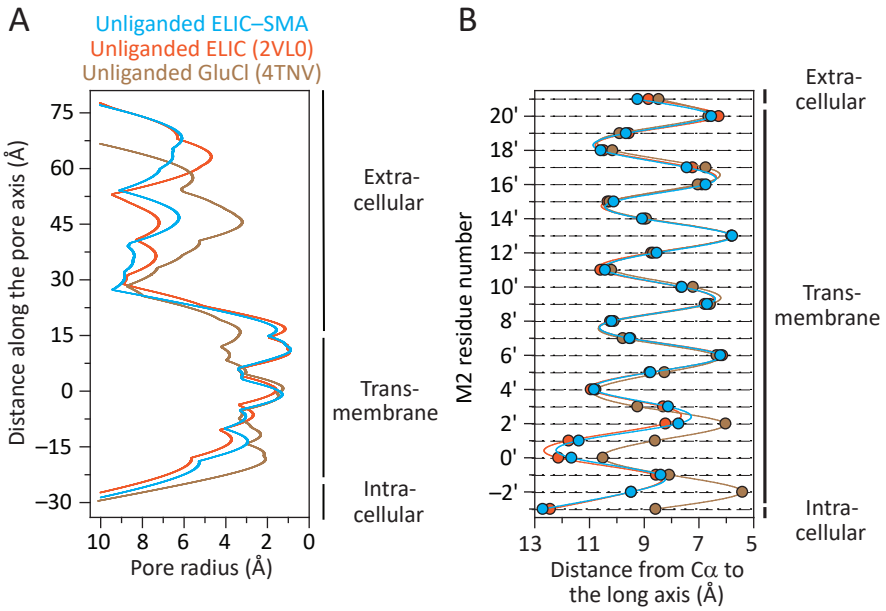

Fig. S5. Pore profiles. The color code is the same for both panels. (*A*) Pore-radius profiles of the indicated atomic models estimated using HOLE (7). The zero-value along the *y*-axis corresponds to the mean position of the Cα atoms of the conserved 9′ leucines. (*B*) Distances between the axis of ion permeation and the Cα atoms for residues in the pore-lining M2 α-helices of the indicated atomic models. M2 residues are denoted using the prime-numbering system.

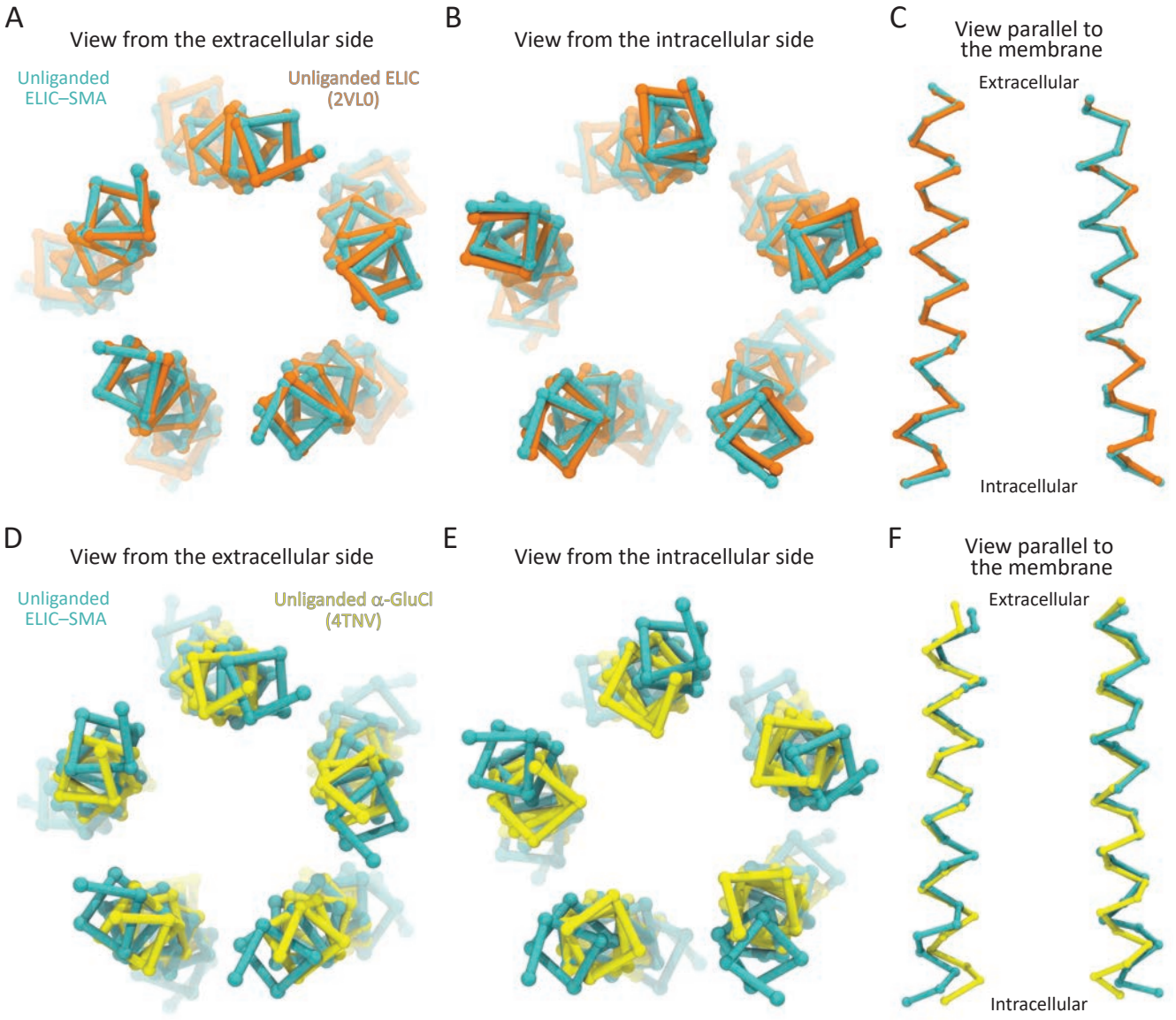

Fig. S6. Superposition of pore-lining M2 α-helices (position –3′ to position 21′). (*A*–*F*) Pairwise superposition of unliganded ELIC–SMA and two X-ray crystal structures: unliganded ELIC (PDB ID: 2VL0; 8) and unliganded α-GluCl (PDB ID: 4TNV; 9). The atomic models were superposed in such a way as to minimize the Cα–Cα distance between aligned residues; they are displayed in trace representation, and the location of Cα atoms is indicated with spheres. For clarity, in *C* and *F*, only two non-adjacent subunits are displayed. Molecular images were prepared with VMD (10).

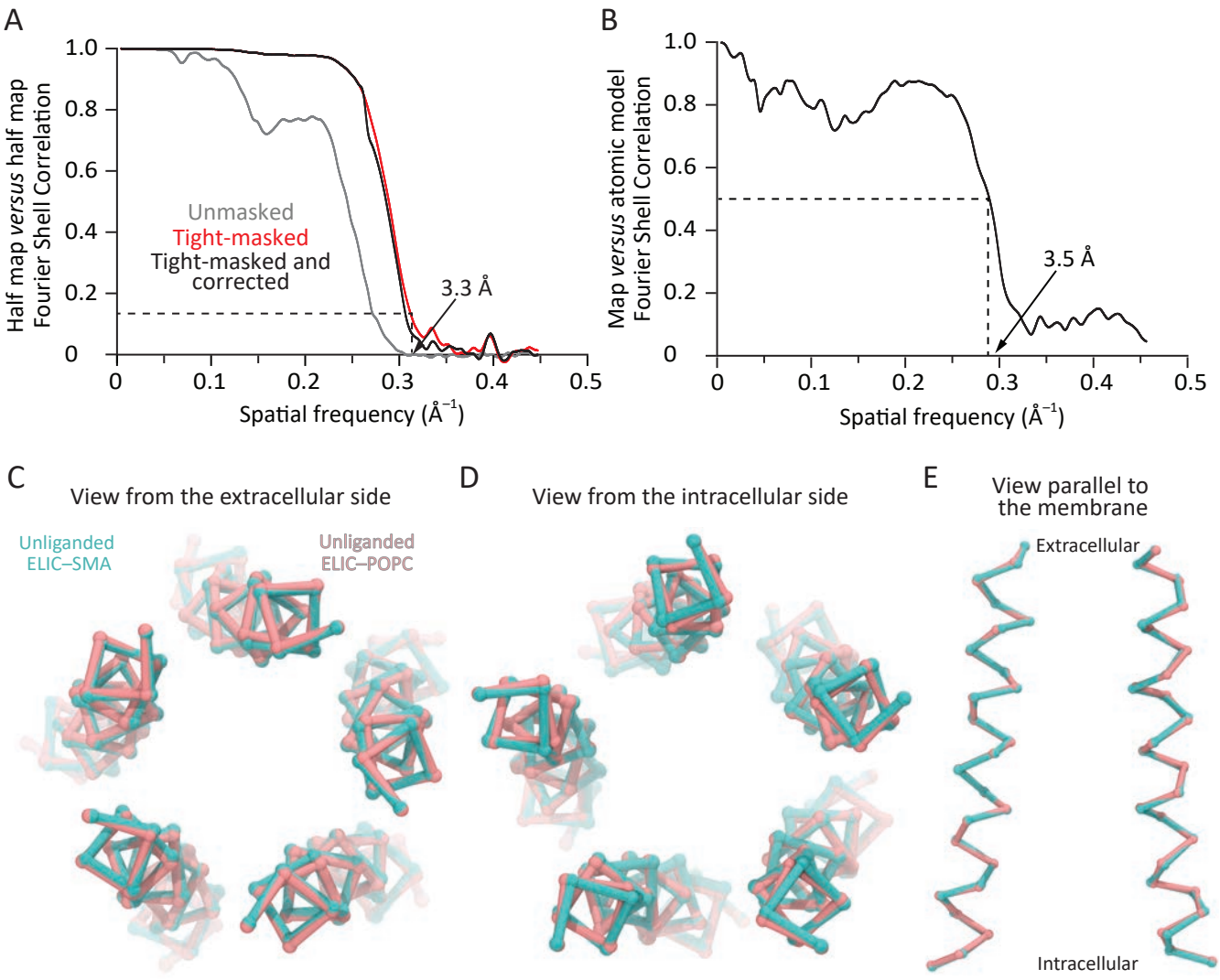

Fig. S7. Unliganded ELIC in POPC-only nanodiscs. Improved 3D reconstruction of detergent-solubilized ELIC reconstituted into POPC-only nanodiscs in the absence of ligands. (*A*) FSC curves computed between independently refined half maps (gold-standard procedure). The global resolution was estimated using the 1/7 (≈ 0.143) cut-off criterion (1) upon application of a tight soft-edged mask and high-resolution noise substitution (2). (*B*) FSC curve computed between the sum of experimental half maps and a noise-free map calculated from the ELIC–POPC atomic model. A soft-edged mask was applied to the experimental map before computation of the curve. The resolution at which the map–model FSC equals 0.5 (3.5 Å) is similar to the global resolution of the 3D reconstruction calculated from the half maps (3.3 Å), as expected from the theoretical relationship between full maps, half maps, noiseless maps, and correctly built atomic models (1). (*C–E*) Superposition of pore-lining M2 α-helices (position –3′ to position 21′) of unliganded ELIC–SMA and unliganded ELIC–POPC. The models were superposed in such a way as to minimize the Cα–Cα distance between aligned residues; they are displayed in trace representation, and the location of Cα atoms is indicated with spheres. For clarity, in *E*, only two non-adjacent subunits are displayed. Molecular images were prepared with VMD (10).

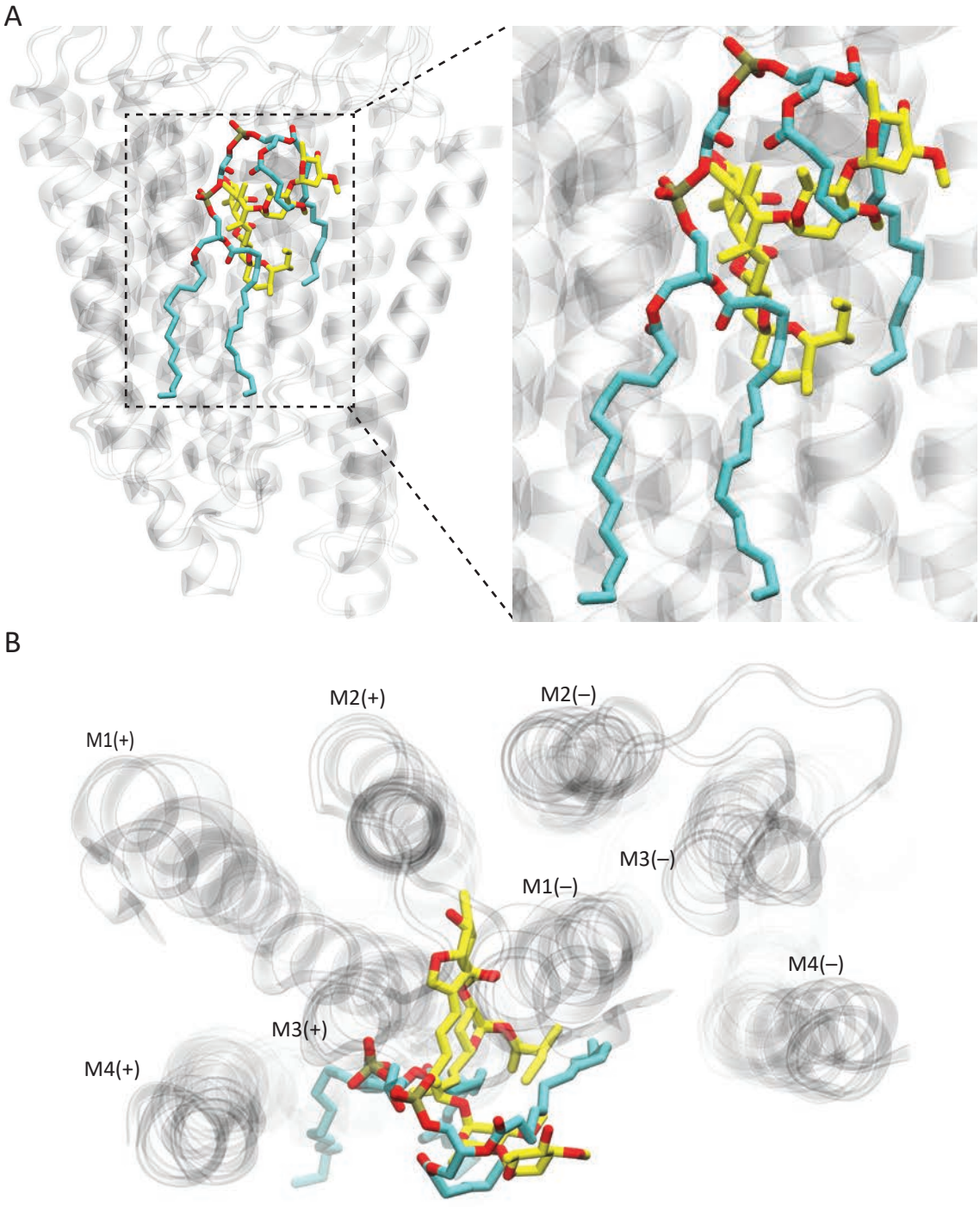

Fig. S8. The cardiolipin-binding site in ELIC overlaps with ivermectin's in α-GluCl. (*A*, *B*) Different views of the structural alignment of the atomic models of unliganded ELIC–SMA and ivermectin-bound α-GluCl (PDB ID: 3RIF; 11). Cardiolipin (cyan-colored carbon atoms) and ivermectin (yellow-colored carbon atoms) are displayed in stick representation. The two proteins are displayed in ribbon representation, in ghost mode, using the same color (gray). "+" and "–" denote the "principal" and "complementary" subunits, respectively. Molecular images were prepared with VMD (10).

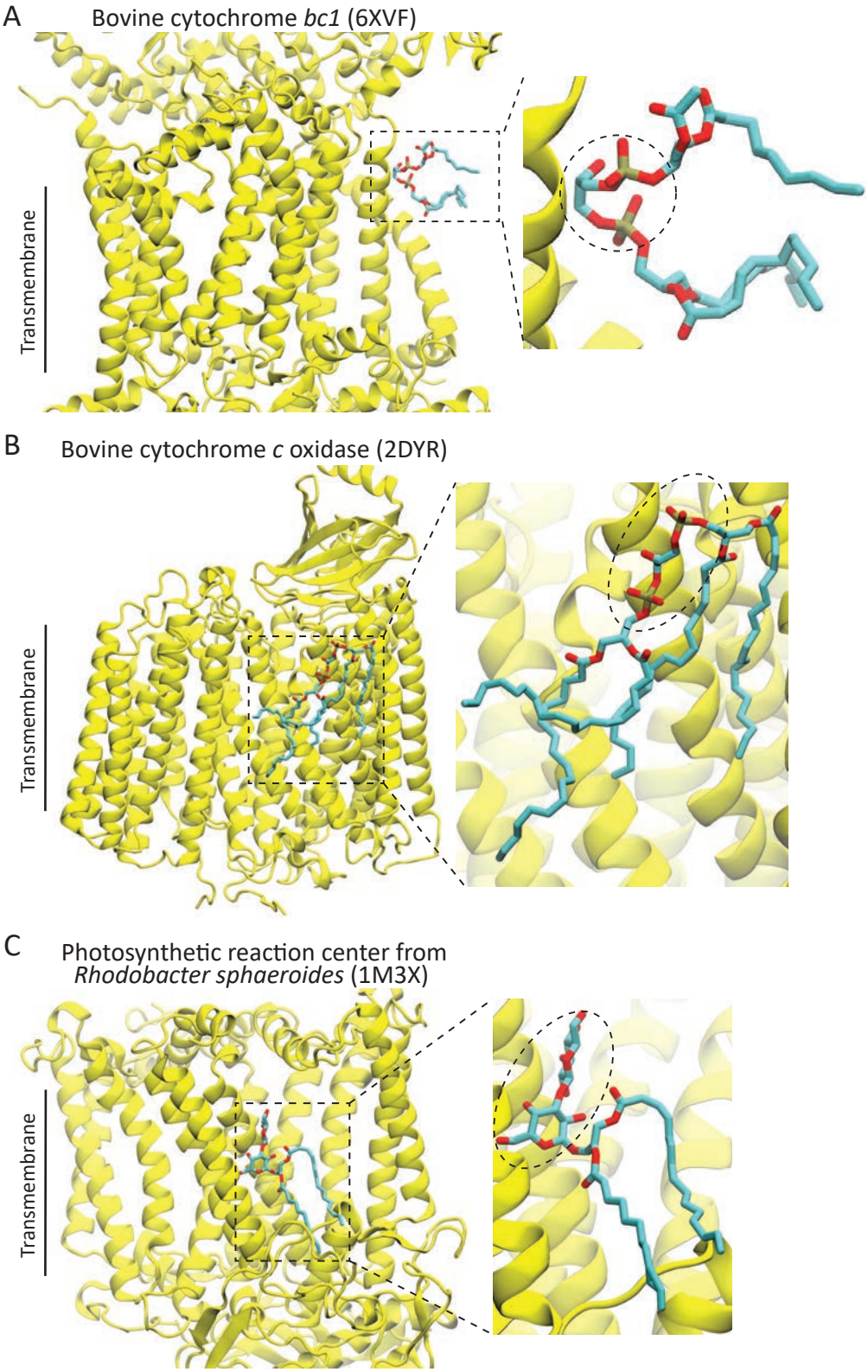

Fig. S9. Non-bilayer conformations and locations of firmly bound lipids in other membrane proteins. Proteins are displayed in ribbon representation; lipids, in stick. (*A*) Cardiolipin in the X-ray crystal structure of bovine cytochrome *bc1* (PDB ID: 6XVF; resolution = 3.50 Å; ref. 12). A dashed-line circle highlights the phosphate–glycerol–phosphate polar head group. (*B*) Cardiolipin in the X-ray crystal structure of bovine cytochrome *c* oxidase (PDB ID: 2DYR; resolution = 1.80 Å; ref. 13). A dashed-line oval highlights the phosphate–glycerol–phosphate polar head group. (*C*) Glucosylgalactosyl diacylglycerol in the X-ray crystal structure of the photosynthetic reaction center from *Rhodobacter sphaeroides* (PDB ID: 1M3X; resolution = 2.55 Å; ref. 14). A dashed-line oval highlights the disaccharide head group. Molecular images were prepared with VMD (10).

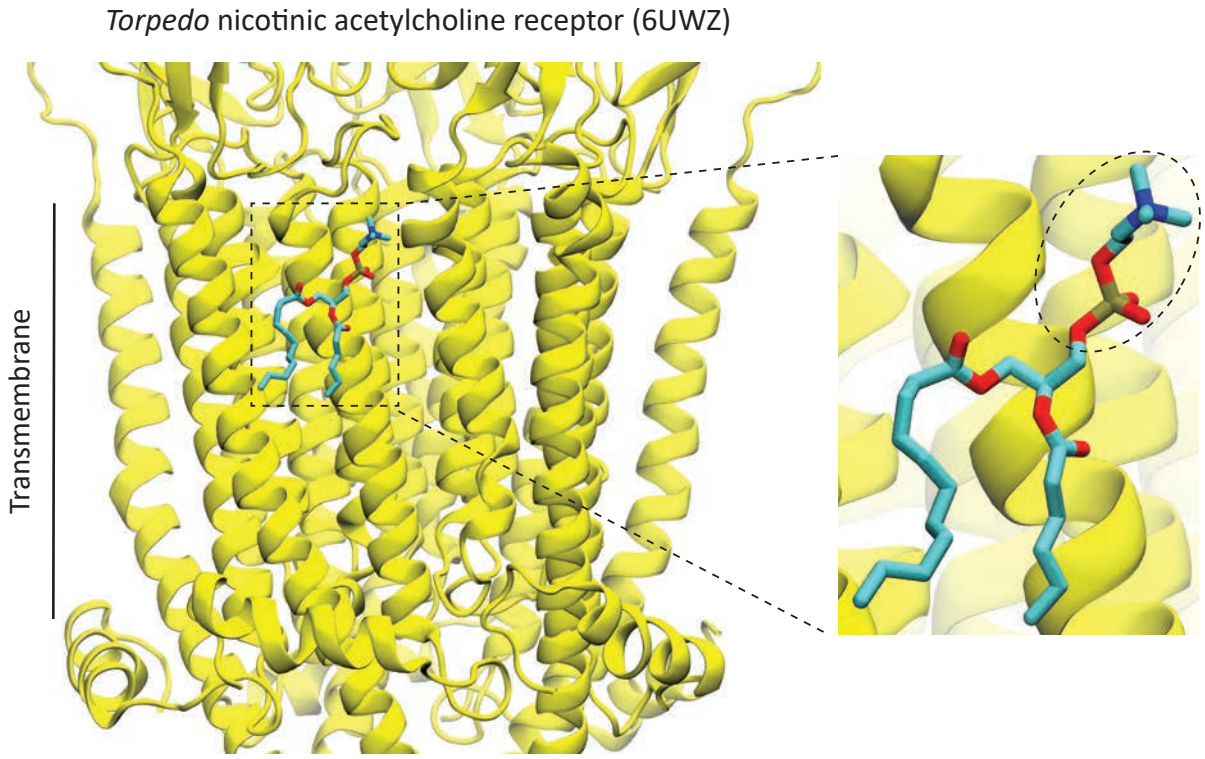

Fig. S10. Non-bilayer conformation and location of a firmly bound lipid in the muscle-type AChR. Phosphatidylcholine bound to the β1 subunit in the cryo-EM structure of the *Torpedo* AChR (PDB ID: 6UWZ; resolution = 2.69 Å; ref. 15). The protein is displayed in ribbon representation; the lipid, in stick. A dashed-line oval highlights the phosphocholine polar head group. Molecular images were prepared with VMD (10).

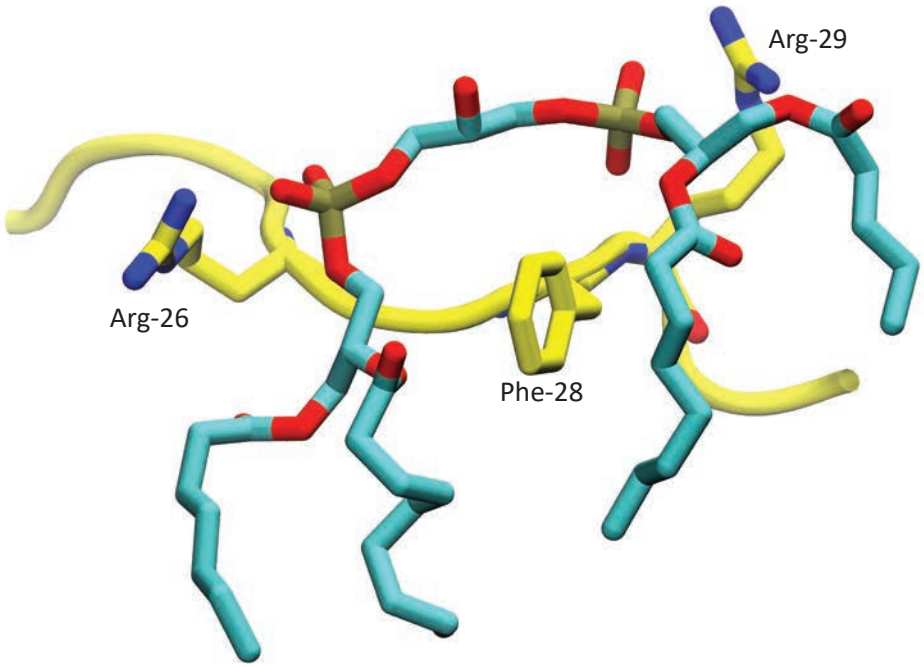

Fig. S11. Residues near the head group of cardiolipin in other membrane proteins. Two arginines and one phenylalanine near the phosphate–glycerol–phosphate moiety of a cardiolipin in mitochondrial complex I from the yeast *Yarrowia lipolytica* (PDB ID: 6YJ4; 16). Amino-acid side chains (yellow-colored carbon atoms) and cardiolipin (cyan-colored carbon atoms) are displayed in stick representation. The molecular image was prepared with VMD (10).

Table S1. Cryo-EM data-collection, processing, and model-refinement statistics

Sample	Unliganded ELIC in SMA nanodiscs	Unliganded ELIC in POPC-only nanodiscs
Data collection		
Grids	Holey carbon	Carbon lacey nanowire
Vitrification method	Leica EM GP2	Spotiton
Microscope	Krios	Krios
Voltage (kV)	300	300
Magnification factor	22,500	45,454
Detector	K2 Summit	K2 Summit
Recording mode	Counting	Counting
Electron-dose rate ($e^{-}Å^{-2}s^{-1}$)	7.06	7.6
Total electron dose ($e^{-}Å^{-2}$)	70.58	63.56
Pixel size (Å)	1.073	1.096
Number of frames	50	50
Total exposure time (s)	10	10
Set defocus range (μm)	–0.3 to 3.3	1.5 to 2.2
EM-data processing		
Number of micrographs	4,639	1,129
Number of picked particles	1,952,324	138,410
Number of particles used for refinement	1,239,532	38,381
Symmetry imposed	C5	C5
Resolution (Å) (half map–half map, FSC threshold = 0.143)	2.5	3.3
Coordinate refinement and validation		
RMSD bonds (Å)	0.008	0.009
RMSD angles (°)	0.610	0.754
Ramachandran favored (%)	92.23	91.26
Ramachandran outliers (%)	0	0
Rotamer outliers (%)	3.96	0.36
Map–model cross correlation (CC, main chain)	0.84	0.83
Clashscore	4.46	6.02
MolProbity score	2.16	1.84
EMRinger score	4.92	3.3
Map–model FSC (Å) (threshold = 0.5)	2.7	3.5

SUPPLEMENTARY REFERENCES

1. P. B. Rosenthal, R. Henderson, Optimal determination of particle orientation, absolute hand, and contrast loss in single-particle electron cryomicroscopy. *J. Mol. Biol.* **333**, 721–745 (2003).

2. S. Chen et al., High-resolution noise substitution to measure overfitting and validate resolution in 3D structure determination by single particle electron cryomicroscopy. *Ultramicroscopy* **135**, 24–35 (2013).

3. J. L. Vilas, *et al.*, MonoRes: Automatic and accurate estimation of local resolution for electron microscopy maps. *Structure* **26**, 337–344 (2018).

4. J. M. de la Rosa-Trevín *et al*., Scipion: a software framework toward integration, reproducibility, and validation in 3D electron microscopy. *J. Struct. Biol.* **195**, 93–99 (2016).

5. E. Ramírez-Aportela, *et al.*, Automatic local resolution-based sharpening of cryo-EM maps. *Bioinformatics* **36**, 765–772 (2020).

6. E. F. Pettersen, *et al.*, UCSF ChimeraX: Structure visualization for researchers, educators, and developers. *Protein Sci.* **30**, 70–82 (2021).

7. O. S. Smart, J. G. Neduvelil, X. Wang, B. A. Wallace, M. S. Sansom, HOLE: a program for the analysis of the pore dimensions of ion channel structural models, *J. Mol. Graph.* **14**, 354–360 (1996).

8. R. J. C. Hilf, R. Dutzler, X-ray structure of a prokaryotic pentameric ligand-gated ion channel. *Nature* **452**, 375–379 (2008).

9. T. Althoff, R. E. Hibbs, S. Banerjee, E. Gouaux, X-ray structures of GluCl in apo states reveal a gating mechanism of Cys-loop receptors. *Nature* **512**, 333–337 (2014).

10. W. Humphrey, A. Dalke, K. Schulten, VMD: Visual Molecular Dynamics. *J. Mol. Graph.* **14**, 33–38 (1996).

11. R. E. Hibbs, E. Gouaux, Principles of activation and permeation in an anion-selective Cys-loop receptor. *Nature* **474**, 54–60 (2011).

12. M. J. McPhillie *et al*., Potent tetrahydroquinolone eliminates apicomplexan parasites. *Front. Cell. Infect. Microbiol.* **10**, 203 (2020).

13. K. Shinzawa-Itoh, *et al.*, Structures and physiological roles of 13 integral lipids of bovine heart cytochrome c oxidase. *EMBO J.* **26**, 1713–1725 (2007).

14. A. Camara-Artigas, D. Brune, J. P. Allen, Interactions between lipids and bacterial reaction centers determined by protein crystallography. *Proc. Natl. Acad. Sci. U. S. A.* **99**, 11055–11060 (2002).

15. M. M. Rahman, *et al.*, Structure of the native muscle-type nicotinic receptor and inhibition by snake venom toxins. *Neuron* **106**, 952-962 (2020).

16. D. N. Grba, J. Hirst, Mitochondrial complex I structure reveals ordered water molecules for catalysis and proton translocation. *Nat. Struct. Mol. Biol.* **27**, 892–900 (2020).